# Construction of dual active sites on diatomic metal (FeCo−N/C-x) catalysts for enhanced Fenton-like catalysis

Zhendong Zhao [a], Wenjun Zhou [a,b,c,*], Daohui Lin [a,b,c], Lizhong Zhu [a,b,c], Baoshan Xing [d], Zhiqi Liu [e]

[a] Department of Environmental Science, Zhejiang University, Hangzhou, Zhejiang 310058, China
[b] Zhejiang Ecological Civilization Academy, Anji, Zhejiang 313300, China
[c] State Key Laboratory of Organic Pollution Process and Control, Zhejiang University, Hangzhou, Zhejiang 310058, China
[d] Stockbridge School of Agriculture, University of Massachusetts, Amherst, MA 01003, USA
[e] Hangzhou Yanqu Information Technology Co., Ltd., Hangzhou, Zhejiang 310003, China

## ARTICLE INFO

## ABSTRACT

High metal loading of single-atom catalysts enables excellent catalytic activity, but possibly causes serious aggregation problem. Herein, a series of diatomic FeCo−N/C-x (x represents metal content) were skillfully designed and applied to improve the catalytic activity for peroxymonosulfate (PMS) activation toward degrading organic micropollutants. The unprecedented dual active sites, referring to Fe(N$_3$)−Co(N$_3$) moiety and FeCo alloy, are constructed on the obtained FeCo−N/C-x, thereby exhibiting significantly greater performance toward degrading aqueous phenol (e.g., 0.316 min$^{-1}$ for FeCo−N/C-3) via PMS activation, compared with those of traditional single-atom Co−N/C (0.011 min$^{-1}$) and Fe−N/C (0.018 min$^{-1}$). Combined experimental and theoretical calculations demonstrate the independent functions of dual active sites, in which Fe(N$_3$)−Co(N$_3$) and FeCo alloy can decrease the energy barrier of O−O bond cleaving resulting in the formation of high-valent FeCo=O reactive species and singlet oxygen, respectively. This study opens up a new platform toward constructing dual active sites for enhanced Fenton-like catalytic activity.

## 1. Introduction

Persulfate-based Fenton-like catalysis has gained widespread application in the remediation of contaminated water because they allow the generation of reactive oxygen species (ROS) such as sulfate radicals (SO$_4^{·-}$), singlet oxygen ($^1$O$_2$), and high-valent metal-oxo complexes [1–6]. Single-atom catalysts (SACs), which are characterized by utmost atomic utilization efficiency, unique electronic structure, and chemical robustness, have exhibited higher performance than their traditional nanoscale transition metal counterparts [7]. Recently, nitrogen-coordinated SACs with metal-nitrogen (M−N) moieties as the crucial active sites have been demonstrated to effectively activate peroxymonosulfate (PMS) or peroxydisulfate (PDS) through unsaturated coordination configuration [8–11]. Specifically, single-atom cobalt or iron catalysts with typical Co−N$_4$ and Fe−N$_4$ sites are observed to catalyze the PMS activation for the generation of ROS [12–15]. Despite the achievements of the SACs in Fenton-like catalysis, single active site in the SACs makes it difficult to circumvent the scaling relationships of

adsorption energies on catalyst surface, i.e., catalytic reaction toward aimed substances is always accompanied by the existence of side reaction, thus leading to a reduction in intrinsic activity [16,17]. Increasing the dosage of SACs can achieve a high catalytic activity to a certain extent, but raises the cost of practical application as well. Therefore, improving the catalytic performance of SACs while decreasing the catalyst dosage is still of scientific significance.

The key factors for improving the catalytic performance of the SACs involve increasing the metal loading to obtain abundant active sites and decreasing the reaction energy barrier to enhance the intrinsic activity of each active site. However, a serious challenge in the former approach is that the high metal loading potentially causes the aggregation of isolated metal atoms into less-active nanoparticles or clusters [8,18]. Recently, diatomic metal catalysts (DAMCs) have emerged as a promising alternative to traditional SACs in order to achieve higher metal loading and more flexible active sites [19]. Over the past decades, DAMCs have been widely applied in the fields of energy, catalysis, and chemical synthesis [20–22]. Notably, during molecular oxygen

---

activation, the formed diatomic metal structure coordinated by nitrogen ($M_1 - M_2 - N$) in DAMCs can significantly elongate the O—O length and thus reduce the energy barrier for the cleavage of the O—O bond compared with that over SACs, which can be considered to enhance their intrinsic activity toward electrocatalytic reactions [23,24]. Analogous to persulfate-based Fenton-like reactions, the cleavage of the O—O bond in the persulfate molecule is a critical process of persulfate activation, which correlates with the performance of catalysts [25]. This inspires us to put forward a reasonable hypothesis that DAMCs are likely to be more effective than SACs for the activation of persulfates, especially the PMS molecule with an asymmetrical peroxide bond. Nevertheless, the application of DAMCs in the Fenton-like catalysis remains in its infancy and there is still a lacking of in-depth exploration on active sites and reaction mechanisms. Particularly, the properties of active sites have a direct effect on the catalytic performance of DAMCs. Therefore, the accurate identification of active sites is of paramount importance to understand the mechanism of PMS activation, and in turn, to facilitate the development of high-activity DAMCs.

Rational construction of DAMCs with abundant active sites to exploit the synergistic effect is fundamental to improve their catalytic activity. Metal–organic frameworks (MOFs), generally constructed by coordinating the metal atoms/clusters with organic ligands, have been employed as ideal precursors to prepare a variety of DAMCs owing to their large surface areas, open channels, and tunable porous structures [26,27]. Because of these advantageous properties, MOFs can also facilitate the uniform and atomic distribution of metal species to achieve high metal loading and to generate multiple active sites. However, the current efforts have been focused on the investigation of major $M_1 - M_2 - N$ active site in DAMCs [28]. Regulating the generation of multiple active sites and unraveling the role of different active sites in PMS activation are important but still poorly understood, which greatly impedes the further application of DAMCs in Fenton-like catalysis.

Among various transition metal single-atom catalysts, Co is found to be highly active for PMS activation [12]. However, the distribution of Co on the earth is less (0.001% in the crust). Moreover, Co is recognized as a toxic metal and the leached Co ions in aqueous solution may cause adverse effect on aqueous media. Comparatively, Fe element has relatively large reserves in the crust and single-atom Fe−N/C has demonstrated excellent activity for PMS activation [13]. Furthermore, introducing Fe into Co−N/C to form diatomic FeCo−N coordination structure can prevent the leaching of Co ions. Therefore, the aim of this study was to construct the dual active sites on diatomic FeCo−N/C-x by precisely adjusting the metal content of the precursors, which was expected to improve the catalytic activity during PMS-based Fenton-like catalysis. First, the obtained catalysts were characterized in order to unveil their morphologies, elemental compositions, coordination structures, and active sites. Then, the catalytic performance was systematically evaluated for phenol degradation by the PMS activation, and further compared with that of traditional single-atom catalysts. In addition, the reactive species generated were identified based on quenching experiment and electron spin resonance. Finally, a dual active sites-dependent activation mechanism was unraveled according to experimental and theoretical calculations. Our study represents a novel breakthrough toward realizing the construction of dual active sites on DAMCs with higher metal loading, which further promotes the development and applications of DAMCs in the field of Fenton-like catalysis.

## 2. Materials and methods

### 2.1. Chemicals and materials

Cobalt(II) chloride ($CoCl_2$), iron(III) chloride ($FeCl_3$), phenol (PN), 4-chlorophenol (4-CP), bisphenol A (BPA), methylparaben (MeP), formic acid ($CH_2O_2$, HPLC grade), phosphoric acid ($H_3PO_4$, HPLC grade), sodium oxalate ($Na_2C_2O_4$), sodium citrate ($C_6H_5Na_3O_7$), humic acid (HA),

*tert*-butyl alcohol (TBA), furfuryl alcohol (FFA), and dimethyl sulfoxide (DMSO) were purchased from Shanghai Aladdin Bio-Chem Technology Co., Ltd. (China). Rhodamine B (RhB), zinc chloride ($ZnCl_2$), sodium sulfite ($Na_2SO_3$), and p-benzoquinone (p-BQ) were obtained from Shanghai Macklin Biochemical Technology Co., Ltd. (China). Formamide (FA), hydrochloric acid (HCl), sodium hydroxide (NaOH), sodium bicarbonate ($NaHCO_3$), and potassium iodide (KI) were purchased from Sinopharm Chemical Regent Co. Ltd. (Shanghai, China). Methyl alcohol (MeOH), acetonitrile (ACN), sulfamethoxazole (SMX), potassium peroxymonosulfate (PMS, $KHSO_5 \cdot 0.5KHSO_4 \cdot 0.5K_2SO_4$), 5,5-dimethyl-1-pyrroline-*N*-oxide (DMPO), 2,2,6,6-tetramethyl-4-piperidone (TEMP), methyl phenyl sulfoxide (PMSO), and methyl phenyl sulfone ($PMSO_2$) of HPLC grade were purchased from Sigma-Aldrich. Deuteroxide ($D_2O$) were purchased from Ningbo Cuiying Chemical Co., Ltd. Unless otherwise specified, all reagents were of analytical grade and used as received without further purification. Deionized water (18.2 MΩ/cm) from a Milli-Q purification system was used for the whole experiments.

### 2.2. Preparation of N/C, Fe−N/C, Co−N/C, and FeCo−N/C-x

Typically, 0.45 mmol $FeCl_3$, 0.45 mmol $CoCl_2$ and 17.1 mmol $ZnCl_2$ were dissolved in 180 mL FA under sonication for 45 min to obtain a homogeneous solution. The addition of $ZnCl_2$, which has a low boiling point and gradually evaporates under high temperature, can lower the concentration of metal atoms and prevent them from aggregation, further promoting the formation of highly isolated M−N sites. Then the mixed solution was transferred into a 200 mL Teflon-lined autoclave and heated at 180 °C for 12 h. The resulted precipitates were collected by centrifugation at 8000 rpm for 8 min, washed at least three times with ethanol and deionized water, and dried in an oven at 60 °C overnight. Finally, the as-prepared powder was placed in a tube furnace and calcined under flowing nitrogen atmosphere at 900 °C for 1 h with a heating rate of 5 °C/min, and naturally cooled to room temperature. The obtained products were denoted as FeCo−N/C-1 and stored in dark. Similarly, FeCo−N/C-2, FeCo−N/C-3, and FeCo−N/C-4 were synthesized following the same protocol of FeCo−N/C-1 except adjusting molar ratios of $ZnCl_2/(FeCl_3 + CoCl_2)$ to 9:1, 4:1, and 3:1, respectively. The addition amounts of $ZnCl_2$, $FeCl_3$, and $CoCl_2$ in different catalysts are listed in Table S1. Besides, metal-free N/C, Fe−N/C, Co−N/C were prepared with the same protocol, except without adding $FeCl_3$ and $CoCl_2$, adding only $FeCl_3$ or $CoCl_2$, respectively.

### 2.3. Characterizations

The surface morphologies and structures of catalysts were observed by scanning electron microscopy (SEM, Gemini SEM 300) and high-resolution transmission electron microscopy (HR-TEM, Thermo Fischer Talos F200x) equipped with energy-dispersive X-ray (EDX) spectroscopy at an accelerating voltage of 200 kV. Aberration-corrected high-angle annular dark-field scanning transmission electron microscopy (HAADF-STEM) images were obtained on a JEM-ARM200F TEM/STEM with a FEI Titan Cubed Themis G2300. The crystalline structures of the catalysts were performed by powder X-ray diffraction (Bruker D8 Advance) with Cu Kα radiation (λ = 0.154 nm at a scan rate of 2°/min in a 2θ range from 5° to 80°. X-ray photoelectron spectroscopy (XPS) was recorded on a Thermo Electron ESCALAB 250XI spectrometer with an Al Kα radiation source, and the binding energy (BE) was calibrated by the C 1 s spectrum at 284.8 eV. The specific surface area was measured based on the Brunauer Emmett Teller (BET) $N_2$ adsorption method (Nova 3000, Quantachrome). The contents of Fe and Co in the prepared catalysts were detected by an inductively coupled plasma mass spectrometer (ICP-MS NexION 300X, PerkinElmer) after a digestion treatment.

X-ray absorption fine structure (XAFS) spectra were collected at the TPS44 A beamline of the National Synchrotron Radiation Research Center (Taiwan, China). The Fe and Co K-edge XANES data were recorded in a fluorescence mode and the references (Fe foil, FePc, Co

foil, CoPc) were recorded in a transmission mode. The storage ring was operated at the electron energy of 3 GeV with a maximum current of 400 mA. The obtained extended X-ray absorption fine structure (EXAFS) data were processed in Athena module (version 0.9.26). Then Fourier transformed fitting was carried out in Artemis (version 0.9.26). The $k^3$ weighting, k-range of 3 – ~12 $Å^{-1}$ and R range of 1 – ~3 Å were used for the fitting. The four parameters, coordination number, bond length, Debye-Waller factor and $E_0$ shift (CN, R, $\sigma^2$, $\Delta E_0$) were partially fixed. For wavelet transform analysis, the $\chi$ (k) exported from Athena was imported into the Hama Fortran code. The parameters were listed as follows: R range, 0 – 6 Å, k range, 3 – 13.9 $Å^{-1}$; k weight, 3; and Morlet function with $\kappa = 10$, $\sigma = 1$ was used as the mother wavelet to provide the overall distribution.

### 2.4. Experimental Procedures

Degradation of organic micropollutants was conducted in a 250 mL beaker under magnetic stirring at 25 °C. In a typical experiment, 5 mg of catalyst was added into 100 mL of PN solution (0.165 mM) and shaken for 30 min to reach the adsorption-desorption equilibrium. The initial pH of solution was maintained at 7.0. Then the degradation reaction was initiated by adding PMS aqueous solution (0.4 g $L^{-1}$). At predetermined time intervals, 1 mL of aliquots were immediately withdrawn, filtered, and quenched with 0.5 mL of sodium sulfite for subsequent HPLC detection. In the cycling experiment, the catalyst was collected after each run by filtration, followed by washing with ethanol and water at least five times, and dried before the next cycling. Degradation experiment in actual water collected from Qizhen Lake (30°18′1″N, 120°5′13″E) and West Lake (30°14′45″N, 120°8′30″E) was performed to assess the practical application of catalysts. Most of experiments were conducted in triplicates, and the mean values with standard deviations were presented in the Figures.

### 2.5. Analytical methods

The concentration of organic pollutants was determined by high-performance liquid chromatography (HPLC, Ultimate 3000, Thermo Fisher, USA) equipped with an Agilent Eclipse XDB-C18 reversed-phase column (4.6 × 150 mm, 5 mm, Supelco) and a UV detector with a column temperature of 25 °C. Detection conditions were presented in Table S2. The PMS concentration was measured on the basis of a KI spectrophotometric method. Total organic carbon was measured by a TOC-VCPH analyzer (Shimadzu, Japan). The amount of leached Fe and Co was measured by an inductively coupled plasma mass spectrometer (ICP-MS NexION 300X, PerkinElmer). Free radicals ($SO_4^{·-}$ and $^·OH$) and singlet oxygen ($^1O_2$) were detected by electron spin resonance (ESR, Bruker A300) spectrometer with 5,5-dimethyl-1-pyrroline-*N*-oxide (DMPO) and 2,2,6,6-tetramethyl-4-piperidone (TEMP) as trapping agents, respectively.

### 2.6. DFT calculations

DFT calculations were performed based on the Vienna Ab initio Simulation Package (VASP) with the generalized gradient approximation (GGA) using the Perdew-Burke-Ernzerhof (PBE) exchange-correlation potential [29–31]. The projected augmented wave (PAW) potential was used to describe the core electrons [32]. The valence/outer-core electrons that are included in the self-consistent-field calculations are listed inter parentheses for each atom: Fe ($3d^6$ $4s^2$), Co ($3d^7$ $4s^2$), K ($3s^2$ $3p^6$ $4s^1$), S ($3s^2$ $3p^4$), O ($2s^2$ $2p^4$), N ($2s^2$ $2p^3$), C ($2s^2$ $2p^2$), and H ($1s^1$). For all optimization calculations, the cutoff energy was set to 420 eV, and K-point was set to Gamma. The convergence criteria for energy and force were set to $10^{-5}$ eV and 0.01 eV/Å, respectively.

## 3. Results and discussion

### 3.1. Catalyst characterization

The crystalline structure, elemental composition, and chemical state of FeCo−N/C-x were determined using X-ray diffraction (XRD) patterns and X-ray photoelectron spectroscopy (XPS). As shown in Fig. S1, all FeCo−N/C-x forms exhibited distinct FeCo alloy signals except FeCo−N/C-1, which was further confirmed by the Fe 2p and Co 2p spectra (Fig. S2, Table S3). The signal gradually strengthened as the doped Fe and Co content increased. No other obvious Fe or Co containing nanocrystals could be found in all FeCo−N/C-x. This result suggests that higher Fe and Co loading are beneficial to promote the formation of FeCo alloy rather than randomly forming Fe and Co nanoparticles or clusters like traditional SACs. The detailed XRD and XPS analyses are provided in the Supporting Information (Text S1).

The morphologies of FeCo−N/C-x were characterized by scanning electron microscopy (SEM), transmission electron microscopy (TEM), high-resolution transmission electron microscopy (HR-TEM), and high-angle annular dark-field scanning transmission electron microscopy (HAADF-STEM). FeCo−N/C-1 exhibited a smooth nanoflower structure with an average diameter of 2 μm (Fig. S3a). With increasing the content of doped Fe and Co, the structure became relatively rough (FeCo−N/C-2 and FeCo−N/C-3) and even collapsed (FeCo−N/C-4), and the surface was partially coated by nanotube-like structures (Fig. S3b–f). The in-situ growth of these nanotubes may be attributed to the transformation of extra metal components into FeCo alloy as understood from the results above. To provide a deeper understanding of the structural transformation, FeCo−N/C-3, which retains the original structure of FeCo−N/C-1 and introduces a new FeCo alloy phase, was chosen for comparison with FeCo−N/C-1. The TEM and HR-TEM images of FeCo−N/C-1 showed the porous graphite-like structures without the formation of obvious particles and crystalline clusters (Fig. 1a–c), implying that Fe and Co atoms are more likely to coordinate with N-doped carbon. The Energy-dispersive X-ray (EDX) mapping of FeCo−N/C-1 suggested that Fe, Co, and N species were homogeneously distributed in the carbon matrix (Fig. 1d). In particular, the distributed bright dots in the HAADF-STEM images and electron energy loss spectroscopy (EELS) mapping corresponding to the signals of Fe and Co atoms exhibited ordered neighboring arrangements (Fig. 1e–g), which confirmed the atomic dispersion of binary Fe−Co sites in FeCo−N/C-1. However, TEM and HR-TEM images of FeCo−N/C-3 clearly showed the two typical lattice spacings of 0.21 nm and 0.34 nm (Fig. 1h and 1i), which were indexed as (110) plane of FeCo alloy and (002) plane of graphitic carbon, respectively [33]. Notably, the FeCo alloy was uniformly coated by a graphitic carbon layer without obvious aggregation, which could prevent metal leaching from the bulk solution. Additionally, multiple small bright dots (Fe and Co signals) in the EDX mapping of FeCo−N/C-3 also demonstrated the existence of diatomic Fe−Co sites (Fig. 1j), but its signal was lower than that of FeCo−N/C-1. On one hand, the extra Fe and Co components weaken the signal intensity of diatomic Fe−Co sites. On the other hand, the existence of FeCo alloy may affect the integrality and stability of diatomic Fe−Co structure as revealed by SEM and TEM images.

X-ray absorption fine structure (XAFS) measurements were performed to probe the atomic structures and coordination configurations of Fe and Co in FeCo−N/C-1 and FeCo−N/C-3. As shown in the Co K-edge X-ray absorption near-edge structure (XANES) spectra (Fig. 2a), the absorption edges of FeCo−N/C-1 and FeCo−N/C-3 were similar to those of CoPc and Co foils, respectively, indicating that the former is more positively charged and exhibits a unique Co−N coordination mode similar to CoPc, whereas the latter mainly contains low-valent Co [34]. Considering that the existence of FeCo alloy may mask the Co−N or Fe−N coordination signal, the Fourier-transformed (FT) $k^3$-weighted extended X-ray absorption fine structure (EXAFS) spectra in R space were analyzed to further reveal the intrinsic coordination structure. As
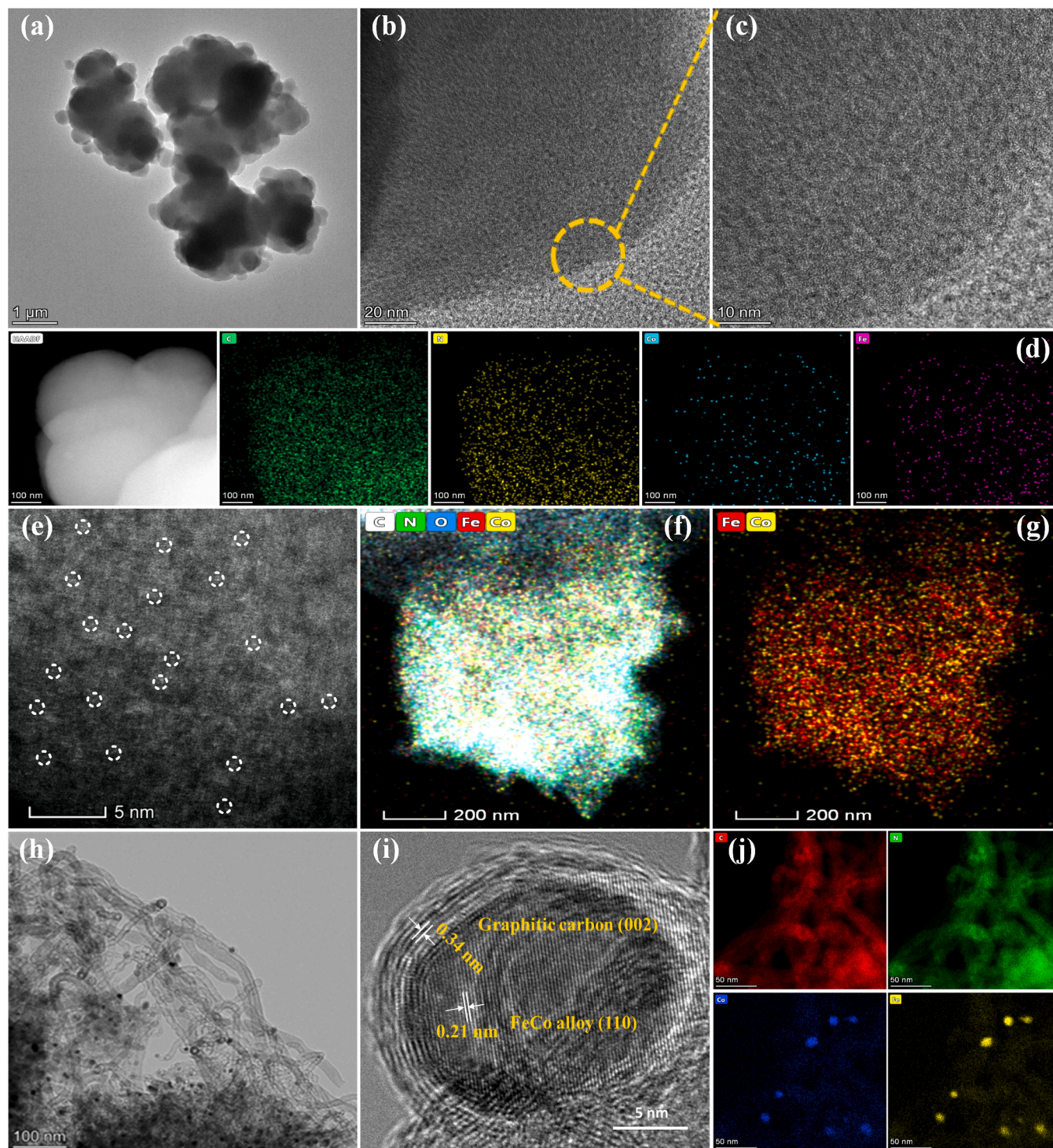
**Fig. 1.** Structure characterization of catalysts. (a) TEM image, (b, c) HR-TEM images, (d) EDX mapping, (e–g) HAADF-STEM images and EELS mapping of FeCo−N/C-1. (h) TEM image, (i) HR-TEM image, and (j) EDX mapping of FeCo−N/C-3.

shown in the Co K-edge EXAFS spectra (Fig. 2b), the first major peak was clearly observed at approximately 1.52 Å, corresponding to the Co−N$_x$ coordination in both FeCo−N/C-1 and FeCo−N/C-3. Meanwhile, the second peak at approximately 2.2 Å verified the formation of metal-metal bonding [23]. Notably, an additional peak at 4.5 Å is assigned to the second shell metal-metal bonding [35], which could be found in FeCo−N/C-3 but was absent in FeCo−N/C-1, indicating that the FeCo alloy only exists in FeCo−N/C-3. In the wavelet transform (WT) plots of Co K-edge EXAFS (Fig. S4a–d), FeCo−N/C-1 showed an

intensity maximum at approximately 5 Å$^{-1}$, corresponding to Co−N coordination [36]. By comparison, the intensity maximum at approximately 8 Å$^{-1}$ in FeCo−N/C-3 can be ascribed to metal-metal bonding [37]. Similar results were also revealed from the Fe K-edge XANES, EXAFS spectra, and WT plots (Fig. 2c and 2d, Fig. S4e–h). In addition, the curve fitting results of the EXAFS spectra further showed that the coordination number of Co−N and Fe−N was nearly three, while that of the first shell metal-metal bonding was only one (Table S4 and S5). Hence, it is reasonable to deduce that the structural model of the
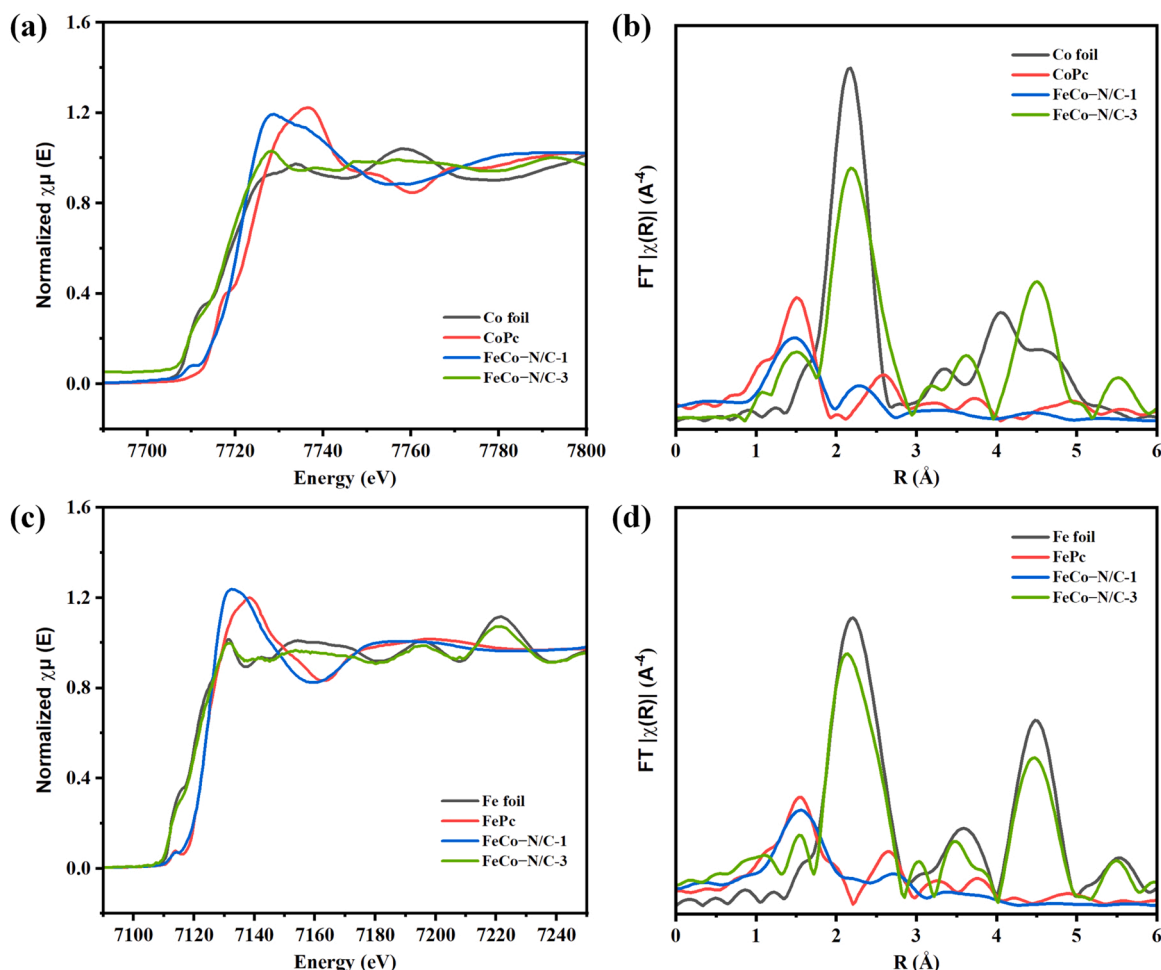
**Fig. 2.** X-ray absorption fine structure of FeCo−N/C-1 and FeCo−N/C-3. (a) Normalized Co K-edge XANES spectra and (b) Fourier-transformed (FT) $k^3$-weighted EXAFS spectra for Co K-edge. (c) Normalized Fe K-edge XANES spectra and (d) Fourier-transformed (FT) $k^3$-weighted EXAFS spectra for Fe K-edge.

diatomic Fe−Co sites should be referred to as "Fe(N₃)−Co(N₃)" shown in Fig. S5. Meanwhile, the XANES and EXAFS spectra of Co−N/C and Fe−N/C also comfirmed the atomically dispersed Co−N₄ and Fe−N₄ coordination structure, respectively (Fig. S6). Therefore, the results above suggest that the active sites of FeCo−N/C-3 mainly consist of FeCo alloy and atomically dispersed Fe(N₃)−Co(N₃) moiety, while that of FeCo−N/C-1 consists of only the latter.

### 3.2. Catalytic performance evaluation

The catalytic performance of FeCo−N/C-x was evaluated for phenol (PN) degradation by the PMS activation. As shown in Fig. S7a, PMS alone was not able to degrade PN because the uncatalyzed PMS activation is relatively inefficient. Moreover, less than 5% of PN could be removed in the absence of PMS, indicating that the adsorption capacity of FeCo−N/C-x was negligible. Notably, metal-free N−C, single-atom Co−N/C and Fe−N/C had relatively poor catalytic activities in the PMS activation, accounting for only 8.3%, 12.6%, and 16.2% removal of PN, respectively (Fig. S7b). However, in the presence of both PMS and FeCo−N/C-x, the removal efficiencies of PN were significantly improved, reaching 35%, 68%, 100%, and 97% within 20 min when catalyzed by FeCo−N/C-1, FeCo−N/C-2, FeCo−N/C-3, and FeCo−N/C-4, respectively (Fig. 3a). Correspondingly, efficient TOC removal could be achieved by FeCo−N/C-1 (44%), FeCo−N/C-2 (58%), FeCo−N/C-3 (78%), and FeCo−N/C-4 (67%), which was the same order as that of the PN degradation (Fig. S8). This result is consistent with the trend of PMS decomposition in different systems. As shown in Fig. S9, PMS is

negligibly decomposed without catalysts. However, PMS decomposition increased to approximately 20%, 28%, 52%, and 38% within 20 min when catalyzed by FeCo−N/C-1, FeCo−N/C-2, FeCo−N/C-3, and FeCo−N/C-4, respectively. These results above suggest that FeCo−N/C-3 is the most desirable catalyst for activating PMS toward the PN degradation. To distinguish the catalytic role of FeCo−N/C-3 against leaching metal ions, homogeneous oxidation by dissolved Fe and Co ions (the same content in FeCo−N/C-3) was conducted. As shown in Fig. S10, leached Fe and Co contributed to approximately 10% removal of PN. Therefore, the highly efficient degradation of PN in the FeCo−N/C-3/ PMS system should be mainly attributed to the heterogeneous oxidation of FeCo−N/C-3.

To test the stability of FeCo−N/C-3, cycling experiment and the effect of pH value on PN degradation were conducted. As shown in Fig. S11, 100% removal of PN could be still achieved within 30 min as the initial pH ranged from 3.5 to 9.1, indicating the high stability of FeCo−N/C-3 over a wide pH range. In the cycling experiment, FeCo−N/C-3 was collected after each run by filtration, followed by washing with copious amounts of ethanol and water, and annealed at 650 °C for 1 h in N₂ to regenerate catalytic activity before the next cycling. In comparison with fresh FeCo−N/C-3, which was capable of completely degrading PN within 60 min, the degradation efficiency of spent FeCo−N/C-3 still reached approximately 91% after five successive cycles (Fig. S12a), far higher than 36% degradation efficiency of spent FeCo−N/C-1 after five cycles (Fig. S12b). The amount of leached Fe and Co in FeCo−N/C-3/ PMS system was determined to be 0.17 and 0.15 mg L⁻¹, respectively, which is below the permissible limit (Fe: 0.3 mg L⁻¹, Co: 1 mg L⁻¹)
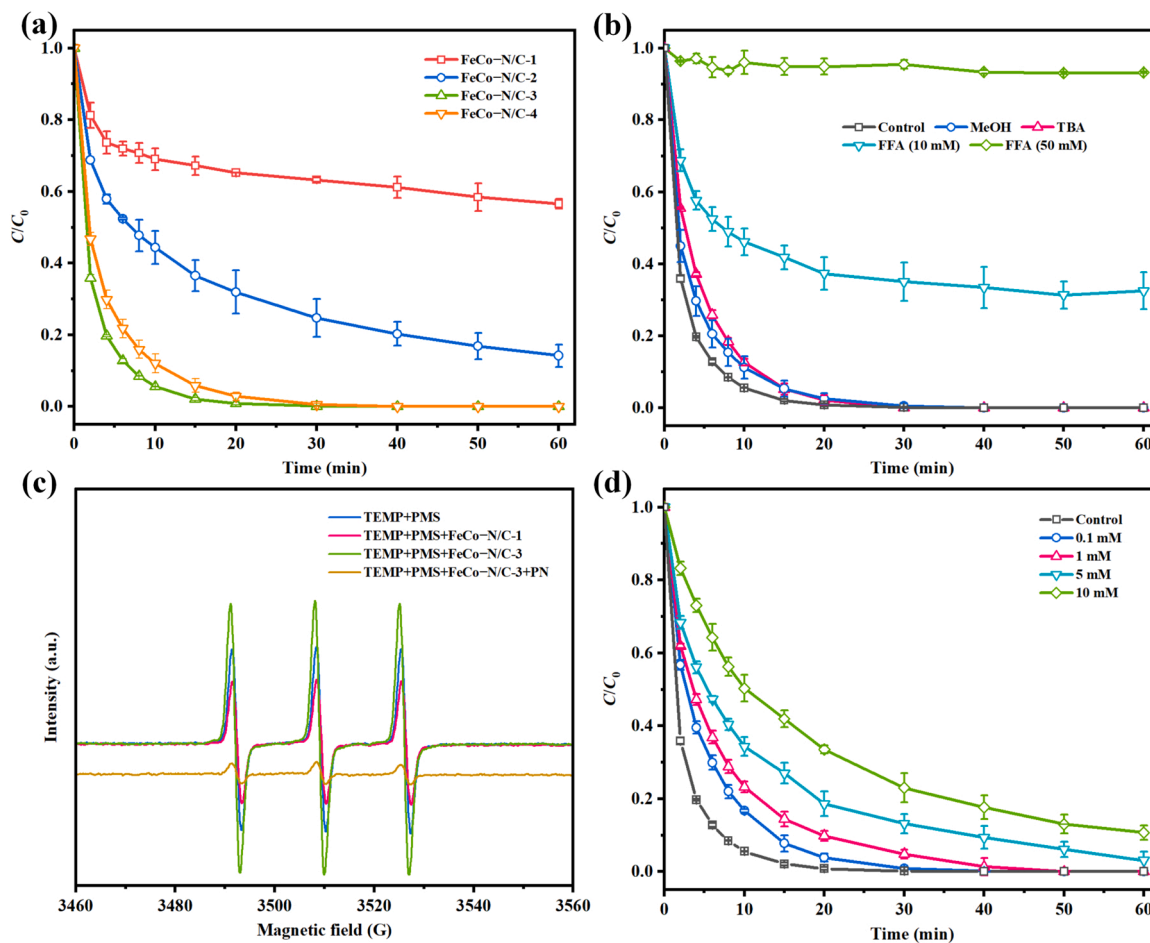
**Fig. 3.** (a) The PN degradation in different catalysts activated PMS systems. (b) The PN degradation in FeCo−N/C-3/PMS system under different quenching conditions. (c) ESR spectra of $^1O_2$ in different systems with TEMP as trapping agent. (d) Effect of DMSO on PN degradation in the FeCo−N/C-3/PMS system. Reaction condition: [PN] = 0.163 mM, [catalyst] = 0.05 g L$^{-1}$, [PMS] = 0.4 g L$^{-1}$, [MeOH] = [TBA] = 650 mM, [DMSO] = 0.1–10 mM, $T$ = 298 K, initial pH = 7.

specified in the Environmental Quality Standards for Surface Water of China (GB3838–2002). Additionally, by comparing the SEM images and XRD spectra of the spent FeCo−N/C-3 with fresh FeCo−N/C-3, the surface morphologies and crystalline structures of the catalysts did not vary significantly before and after the cycling experiments (Fig. S13). Moreover, FeCo−N/C-3/PMS system also exhibits a high degradation efficiency for different organic micropollutants such as bisphenol A (BPA), p-chlorophenol (4-CP), methylparaben (MeP), rhodamine B (RhB), and sulfamethoxazole (SMX) (Fig. S14). Based on the results above, FeCo−N/C-3/PMS system has outstanding stability and shows great potential for practical applications.

To further compare the catalytic performance, the apparent rate constants (k) of these catalysts were calculated using the pseudo-first-order kinetic model. As shown in Fig. S15 and Table S6, all the catalysts showed varying catalytic activities for PN degradation. Specifically, the k values for FeCo−N/C-x were significantly higher than those of metal-free N − C, single-atom Co−N/C and Fe−N/C, whic can be ascribed to the higher metal loading (1.19 wt% ~ 14.33 wt% Fe + Co for FeCo−N/C-x vs. 0.68 wt% Co for Co−N/C and 0.87 wt% Fe for Fe−N/C). The best catalytic performance was obtained for FeCo−N/C-3 with a k value of 0.316 min$^{-1}$, followed by 0.234 min$^{-1}$, 0.095 min$^{-1}$, and 0.029 min$^{-1}$ for FeCo−N/C-4, FeCo−N/C-2, and FeCo−N/C-1, respectively. Noticeably, the k values of FeCo−N/C-3, FeCo−N/C-4, and FeCo−N/C-2 are 9.9, 7.1, and 2.3 times as high as that of FeCo−N/C-1, respectively. The results above indicate that the catalytic performance of dual-active-sites catalysts (e.g., FeCo−N/C-3) far outweighs that of single-active-site catalysts (e.g., FeCo−N/C-1).

It is known that specific surface area and metal loading of catalyst are also important factors for determining the catalytic activity [7,38]. Thus, the structure-property relationships of the catalytic performance with the surface area and bulk metal content of FeCo−N/C-x were investigated. A poor correlation coefficient ($R^2$ = 0.53) was observed between the k values and surface area (Fig. S16a), suggesting that the specific surface area may not be an important factor in the PMS activation for PN removal. By contrast, the catalytic performance of FeCo−N/C-x correlates well with their Fe + Co content ($R^2$ = 0.90, Fig. S16b). It should be noted that the higher metal loading for FeCo−N/C-x (x = 1, 2, 3) clearly indicates the better catalytic activity, suggesting that FeCo alloy serving as active site plays a crucial role in determining the catalytic activity. However, the maixmum metal loading for FeCo−N/C-4 (14.33 wt%) does not necessarily result in the best catalytic activity, probably because the excess FeCo alloy destroys the intrinic structure of Fe(N$_3$)−Co(N$_3$) sites. It is very likely that the low k value for FeCo−N/C-1 misleads the significance of Fe(N$_3$)−Co(N$_3$) moiety, but 48% removal of PN and 44% removal of TOC in the FeCo−N/C-1/PMS system within 60 min prove the importance of Fe(N$_3$)−Co(N$_3$) active site. More strikingly, varying the Fe/Co ratio of FeCo−N/C-x was not conductive to the improvement of catalytic activity, and the best ctalytic activity was achieved with the Fe/Co ratio of 1:1 (Fig. S16c). According to the results above, both Fe(N$_3$)−Co(N$_3$) moiety and FeCo alloy are responsible for the high catalytic activity of FeCo−N/C-x. Although it is rather difficult to quantify the contribution of Fe(N$_3$)−Co(N$_3$) moiety and FeCo alloy to the catalytic degradation of PN, these results highlight the critical role of the dual active sites of the

catalysts in the PMS-activated oxidation process.

Very intriguingly, the catalytic activities of FeCo−N/C-x in PMS activation were compared with the recently reported SACs with single active site (Table S7). It is impressive to notice that $k$ values of FeCo−N/C-3 with dual active sites are higher than those of traditional SACs such as Fe SAC, Co SAC, and Cu SAC, even though using less catalyst dosage than SACs. This result further emphasizes the significance of dual active sites and suggests that diatomic catalysts with higher metal loading are effective in preventing the metal aggregation and may have a broader perspective on PMS-based Fenton-like catalysis.

### 3.3. Identification of reactive species

Radical quenching experiments were performed to identify the reactive species involved in the PN degradation. FeCo−N/C-1 and FeCo−N/C-3 were chosen for the following experiments. Generally, sulfate ($SO_4^{\cdot-}$) and hydroxyl (·OH) radicals have been proposed as the dominant reactive species in the PMS-based Fenton-like reactions. MeOH was used as a scavenger for both $SO_4^{\cdot-}$ and·OH ($k_{SO4\cdot-} = 3.2 \times 10^6$ $M^{-1}$ $s^{-1}$, $k_{\cdot OH} = 9.7 \times 10^8$ $M^{-1}$ $s^{-1}$), while TBA was only effective for·OH ($k_{\cdot OH} = 3.8 \times 10^8$ $M^{-1}$ $s^{-1}$ − $7.6 \times 10^8$ $M^{-1}$ $s^{-1}$) [39,40]. As shown in Figs. S17 and 3b, both MeOH and TBA, even at 500 times the molar concentrations of PMS, did not exhibit apparent inhibition on the PN degradation in the FeCo−N/C-1/PMS and FeCo−N/C-3/PMS system, indicating that $SO_4^{\cdot-}$ and·OH was not the main reactive species during the reaction. When furfuryl alcohol (FFA) (10–50 mM), an effective scavenger for singlet oxygen ($k^1_{O2} = 1.2 \times 10^8$ $M^{-1}$ $s^{-1}$) [41], was applied to the FeCo−N/C-1/PMS system, an insignificant inhibition effect on the PN degradation was observed (Fig. S17). By contrast, over the FeCo−N/C-3/PMS system, the PN degradation was apparently inhibited after adding an equal molar concentration of FFA, with removal efficiency decreasing from 68% to 7% (Fig. 3b). Considering that FFA was not able to decompose either PMS (Fig. S18a) or PN (Fig. S18b), $^1O_2$ is thus considered to be involved in the PN degradation in the FeCo−N/C-3/PMS system, while other reactive species generated in the FeCo−N/C-1/PMS system may play a crucial role in the PN degradation.

Further, ESR experiments were conducted to detect the generation of reactive species during the PMS activation. As previously reported, 5,5-dimethyl-1-pyrroline-*N*-oxide (DMPO) and 2,2,6,6-tetramethyl-4-piperidone (TEMP) were applied as spin-trapping agents for radicals ($SO_4^{\cdot-}$ and·OH) and $^1O_2$, respectively [42,43]. As shown in Fig. S19, the characteristic signals of DMPO–·OH adducts (1:2:2:1, $\alpha_N = \alpha_H = 14.9$ G) were observed in the absence of catalysts, which is attributed to the hydrolysis of PMS. However, no obvious $SO_4^{\cdot-}$ and ·OH signals but the typical heptet of 5,5-dimethyl-2-oxopyrroline-1-oxyl (DMPOX) adducts (5,5-dimethyl-2-pyrrolidone-N-oxyl, 1:2:1:2:1:2:2:1, $\alpha_N = 7.2$ G, $\alpha_H = 4.1$ G) appeared in the presence of FeCo−N/C-1 and FeCo−N/C-3. It has been proven that DMPO can also be oxidized to DMPOX by other reactive species such as $^1O_2$ and high-valent metal-oxo species [11,12]. Subsequently, TEMP-trapped ESR spectra were used to probe the generation of $^1O_2$. As shown in Fig. 3c, the weak triplet signal of TEMP-$^1O_2$ adducts (1:1:1, $\alpha_N = 16.9$ G) in the TEMP/PMS system might have resulted from the self-decomposition of PMS. However, the intensity of the TEMP-$^1O_2$ signal decreased in the presence of FeCo−N/C-1, suggesting the absence of $^1O_2$ in the FeCo−N/C-1/PMS system. In contrast, the TEMP-$^1O_2$ signal first increased and then decreased after the successive addition of FeCo−N/C-3 and PN. To further confirm the presence of $^1O_2$ in the FeCo−N/C-3/PMS system, deuteroxide ($D_2O$) was used to replace solvent $H_2O$ because of the solvent-specific capacity for quenching of $^1O_2$ ($k_d$ ($H_2O$) = $2.5 \times 10^5$ $s^{-1}$; $k_d$ ($D_2O$) = $1.5 \times 10^4$ $s^{-1}$). As shown in Fig. S20, the intensity of the TEMP-$^1O_2$ signal in the FeCo−N/C-3/PMS system further increased when $D_2O$ was used to replace solvent $H_2O$, which is attributed to the longer lifetime of $^1O_2$ in $D_2O$ (20–32 μs) than $H_2O$ (2 μs) [44]. It can be concluded from all the quenching experiments that $^1O_2$ is generated in the FeCo−N/C-3/PMS

system rather than in the FeCo−N/C-1/PMS system, which plays an important role in the PN degradation.

Recently, it has been widely proposed that high-valent metal-oxo species such as Fe(IV)/Fe(V), Mn(V), and Co(IV) are dominant reactive species/intermediates in Fenton or Fenton-like reactions [45–47]. To verify whether the high-valent metal-oxo species are generated in the FeCo−N/C-1/PMS and FeCo−N/C-3/PMS systems, dimethyl sulfoxide (DMSO) was used as a trapping agent to quench the PN degradation based on the fact that DMSO can be oxidized by high-valent metal-oxo species [48]. Even though DMSO can also be oxidized by radicals, the radical quenching experiments and ESR spectra have ruled out the effect of generation of $SO_4^{\cdot-}$ and·OH in the reaction system. As shown in Figs. S21 and 3d, the PN degradation was significantly decelerated as the DMSO concentration increased from 0 mM to 10 mM, indicating that high-valent metal-oxo species were generated and contributed to the PN degradation in both systems. To obtain a clear quantification of the role of high-valent metal-oxo species, methyl phenyl sulfoxide (PMSO) consumption and methyl phenyl sulfone (PMSO$_2$) generation, which is easily determined by high-performance liquid chromatography-ultraviolet (HPLC-UV) detection, were evaluated in the FeCo−N/C-1/PMS and FeCo−N/C-3/PMS systems. It is known that PMSO can be oxidized by high-valent metals to yield the corresponding PMSO$_2$ via an oxygen atom transfer mechanism [47,49]. These results suggest that the transformation ratio of PMSO to PMSO$_2$ was only 17% when $^1O_2$ served as the exclusive oxidant (Fig. S22a). However, 61.4% of PMSO was consumed in the FeCo−N/C-1/PMS system, which produced an equal molar amount of PMSO$_2$ (Fig. S22b). By comparison, PMSO consumption was higher in the FeCo−N/C-3/PMS system (83.3%) because of the oxidation of $^1O_2$ (Fig. S22c). Nevertheless, the almost 100% transformation ratio of PMSO to PMSO$_2$ in both systems clearly proves that both FeCo−N/C-1 and FeCo−N/C-3 enable the generation of high-valent metal-oxo species by activating PMS.

### 3.4. Dual active sites-dependent activation mechanism

The SACs with $CoN_4$ or $CoN_{2+2}$ sites are reported to be highly reactive for the PMS activation to generate $^1O_2$ [12,36], while high-valent metal-oxo species serving as the active intermediates are predominantly generated in the single-atom Fe catalyst-activated PMS or PDS processes [5,11]. However, there is still a lacking of deep understanding on the active sites of the DAMCs participating in the PMS activation. Herein, the atomically dispersed $Fe(N_3)−Co(N_3)$ moieties, which have a similar coordination structure to the previously reported $CoN_4$ and $FeN_4$ sites, are hypothesized to be active sites for the PMS activation. To confirm this hypothesis, the Fe and Co species of the catalysts were removed from the FeCo−$N_x$ skeleton by immersing it in a 1 M HCl solution. After 24 h of acid treatment, the remaining metal contents in FeCo−N/C-1 and FeCo−N/C-3 declined to only 0.24% and 1.38%, respectively (data from ICP-MS). Correspondingly, the removal efficiencies of PN in the FeCo−N/C-1/PMS and FeCo−N/C-3/PMS systems decreased by 68% and 43% within 60 min, respectively (Fig. S23). To further determine the role of the $Fe(N_3)−Co(N_3)$ active sites, several chelating agents such as oxalate or citrate were added to the FeCo−N/C-1/PMS system because FeCo−N/C-1 consists of only Fe($N_3$)−Co($N_3$) moieties. It has been recognized that the carboxyl group of oxalate and citrate can coordinate with high-valent Fe or Co to form stable metal-carboxyl complexes [50]. If the diatomic Fe($N_3$)−Co($N_3$) moieties are exclusive active sites in the FeCo−N/C-1/PMS system, the addition of oxalate/citrate will impede the PMS activation and subsequent PN degradation. As shown in Fig. S24, the PN degradation was gradually suppressed as the concentration of oxalate/citrate increased to 10 mM. Notably, no obvious decrease in the concentration of oxalate/citrate was observed (Fig. S25), indicating that they were neither adsorbed on the FeCo−N/C-1 surface nor degraded by the FeCo−N/C-1/PMS system. Therefore, the inhibition effect of oxalate/citrate on the PN degradation most likely resulted from the destruction

of the $Fe(N_3)-Co(N_3)$ moieties. Additionally, the PMS decomposition was inhibited after the addition of oxalate/citrate (Fig. S26). Combined with the results of reactive species identification, it is reasonable to consider that the diatomic $Fe(N_3)-Co(N_3)$ moieties are the major active sites mediating the generation of high-valent metal-oxo species rather than $^1O_2$, which results in the degradation of PN.

In addition to high-valent metal-oxo species, $^1O_2$ also exists in the FeCo−N/C-3/PMS system and contributes to the PN degradation. To the best of our knowledge, $^1O_2$ generation is hypothesized to follow several possible pathways: (i) surface carbonyl/ketone groups on carbonaceous catalysts serve as active sites to react with PMS via nucleophilic addition for the formation of $^1O_2$ [51], (ii) the superoxide radical ($O_2^{\cdot-}$) intermediate is converted to $^1O_2$ via recombination or proton-promoted disproportionation [52], and (iii) self-decomposition of PMS mediates the generation of $^1O_2$ by the following reaction: $HSO_5^- + SO_5^{2-} \rightarrow HSO_4^- + SO_4^{2-} + {^1O_2}$ [53]. A set of experiments were carried out to investigate the origin of $^1O_2$. Firstly, the C 1 s and O 1 s XPS spectra of FeCo−N/C-3 ruled out the existence of carbonyl or ketone (C=O) groups on the catalyst surface (Fig. S27). Secondly, p-BQ was selected as a scavenger of $O_2^{\cdot-}$ ($k_{O2.-} = 9.7 \times 10^8$ $M^{-1}$ $s^{-1}$) [54]. Results shown in Fig. S28 suggest that the addition of p-BQ had negligible inhibition on the PN degradation in the FeCo−N/C-3/PMS system, even though the p-BQ concentration increased from 1 mM to 5 mM. Thus, the generation of $^1O_2$ may not have resulted from the recombination or disproportionation of $O_2^{\cdot-}$. Based on the ESR experiments, $^1O_2$ was only present in the FeCo−N/C-3/PMS system rather than in the FeCo−N/C-1/PMS system. Therefore, the most likely active site for $^1O_2$ is considered to be derived from the FeCo alloy in FeCo−N/C-3. Previous studies on the PMS activation by N-doped graphite-encapsulated metal nanoparticles suggested that NiZn alloy could improve the self-decomposition of PMS for the generation of $^1O_2$ [55], thus highlighting the pivotal role of NiZn

alloy as an electron conduction channel. Inspired by this fact, it is believed that FeCo alloy in FeCo−N/C-3 also promotes the PMS activation owing to its superior conductivity.

DFT calculations were employed to distinguish the different reaction pathways and activation mechanisms. The potential energy profiles of the proposed intermediates (INT) for the activation of PMS for the pathway generating high-valent metal-oxo species by $Fe(N_3)-Co(N_3)$ sites are shown in Fig. 4a. Firstly, $Fe(N_3)-Co(N_3)$ sites interacted with PMS to generate the $=FeCo-HSO_5$ complex (INT 1), through an exergonic process with a calculated barrier of − 1.99 eV. Subsequently, proton transfer occurred for INT1, resulting in the formation of $=FeCo-OSO_4$ (INT 2) with an energy barrier of 2.90 eV. The O−O bond of INT 2 underwent heterolytic cleavage with a barrier of only 1.14 eV, which eventually formed the high-valent FeCo=O reactive species responsible for the degradation of organic pollutants. According to the calculation above, the total reaction barrier for the formation of high-valent FeCo=O reactive species was only 2.05 eV, which was far lower than that for the formation of high-valent Fe=O (3.28 eV) and high-valent Co=O (4.54 eV) species (Fig. S29 and S30, Text S2, Table S8), further proving the thermodynamic feasibility of the entire reaction.

To unveil the role of the FeCo alloy in the generation of $^1O_2$, a three-dimensional charge density difference study was conducted to reveal the interaction between FeCo−N/C-3 and PMS. For FeCo−N/C-3, the electron accumulation regions were mainly concentrated in the outer space of the graphite layers, while the electron depletion regions appeared on the surface of the FeCo alloy (Fig. 4b). Two-dimensional valence electron density color-filled maps of the N/C model and FeCo alloy doped N/C model, and Bader charge analysis further confirmed that approximately 1.65 of electrons preferentially flowed from the FeCo alloy toward the N/C plane (Fig. S31). The results above indicate that the FeCo
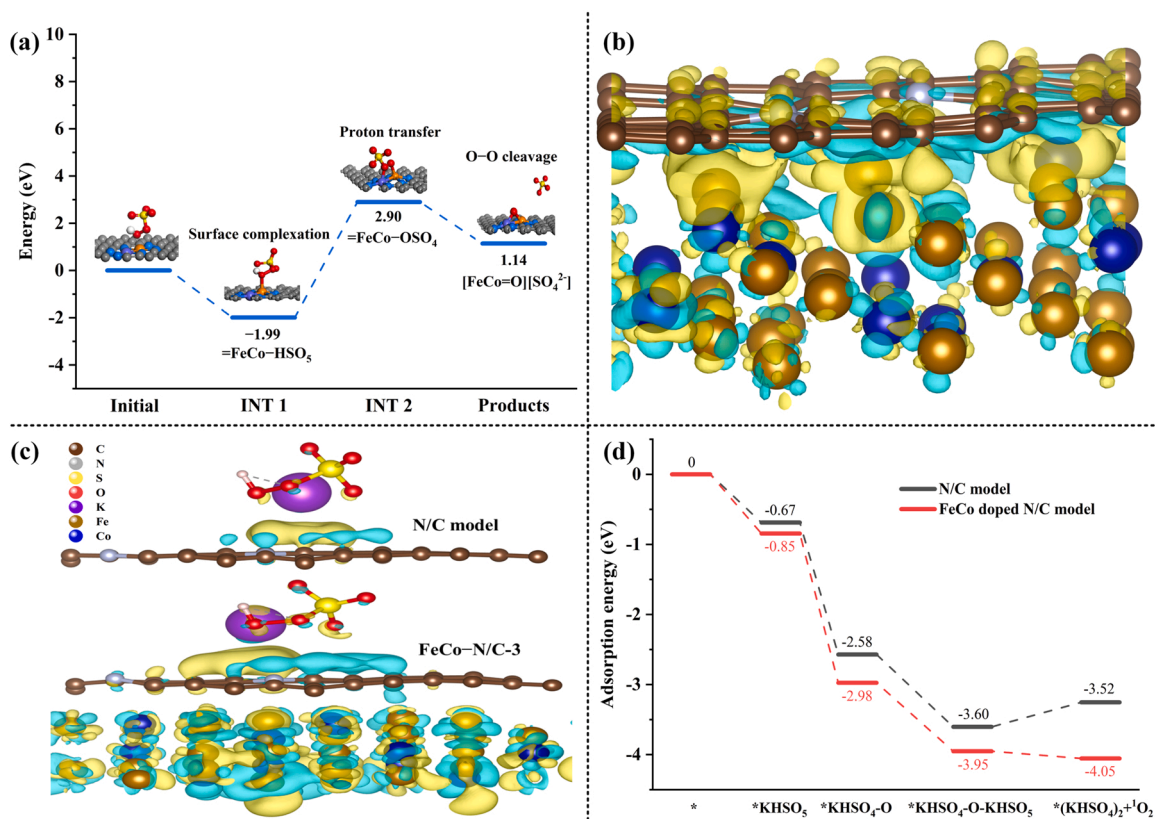


**Fig. 4.** (a) Potential energy profiles of pathway for the generation of high-valent metal-oxo species. (b) Three-dimensional charge density difference of FeCo−N/C-3. (c) The calculated charge density difference diagrams of PMS adsorbed on the N/C model and FeCo−N/C-3. Isosurface contour is 0.0003 $e$/bohr$^3$. The light yellow and light blue correspond to the electron accumulation and electron depletion, respectively. (d) Potential energy profiles of adsorption configuration of PMS for the generation of $^1O_2$.

alloy can not only donate electrons to the interacting graphite layers but can also enhance the electron density of the carbon lattice. When PMS was added, the charge distribution of the carbon layer changed significantly, revealing the chemisorption of PMS on the FeCo−N/C-3 substrate (Fig. 4c). To further elucidate the PMS adsorption on the N/C model and FeCo alloy doped N/C model, the optimized geometric structure of the adsorption configuration of PMS and calculated adsorption energy ($E_{ads}$) are shown in Fig. 4d and Fig. 5. Clearly, the evolution of $^1O_2$ by the self-decomposition of PMS was exergonic and spontaneous. Compared with the N/C model, the FeCo alloy doped N/C model exhibited lower $E_{ads}$ of − 4.05 eV. It should be noted that in the transformation process from *KHSO$_4$−O−KHSO$_5$ to *(KHSO$_4$)$_2$ + $^1O_2$, $E_{ads}$ began to increase from − 3.60 eV to − 3.25 eV for the N/C model, signifying that the adsorption probability of *KHSO$_4$ −O−KHSO$_5$ was relatively low. By contrast, $E_{ads}$ continued to decrease from − 3.95 eV to − 4.05 eV for the FeCo alloy doped N/C model. These results suggest that the FeCo alloy enables the reduction of the $E_{ads}$ of PMS on the N/C model by providing electrons for the carbon lattice, which facilitates the PMS activation and self-decomposition for the generation of $^1O_2$. Combining the above discussions, a dual active sites-dependent activation mechanism is systematically unraveled. As shown in Scheme 1, over

the FeCo−N/C-x, the Fe(N$_3$)−Co(N$_3$) moiety is beneficial for the cleavage of O−O bond leading to the generation of high-valent FeCo=O species, while the FeCo alloy enables the PMS adsorption via enhanced electron transfer, thus promoting the PMS self-decomposition for the generation of $^1O_2$. The independent functions of dual active sites can unprecedentedly decrease the energy barrier of O−O bond cleaving of PMS for boosting Fenton-like catalytic activity.

### 3.5. Environmental resistance of FeCo−N/C-3/PMS system

In a real water matrix, the overall efficiency of the Fenton-like reaction is more susceptible to interference by common background constituents. To verify the feasibility of the FeCo−N/C-3/PMS system in practical applications, the effects of various inorganic anions (Cl$^-$, NO$_3^-$, and HCO$_3^-$) and dissolved organic matter such as humic acid (HA) on the PN degradation were investigated. As shown in Fig. 6 and Text S3, although the background water constituents had a certain degree of effect on the Fenton-like reaction, the overall efficiency of the PN degradation still reached 100% within 60 min, which suggests that the FeCo−N/C-3/PMS system is highly resistant to complex water matrices. More importantly, highly efficient PN degradation was also achieved in
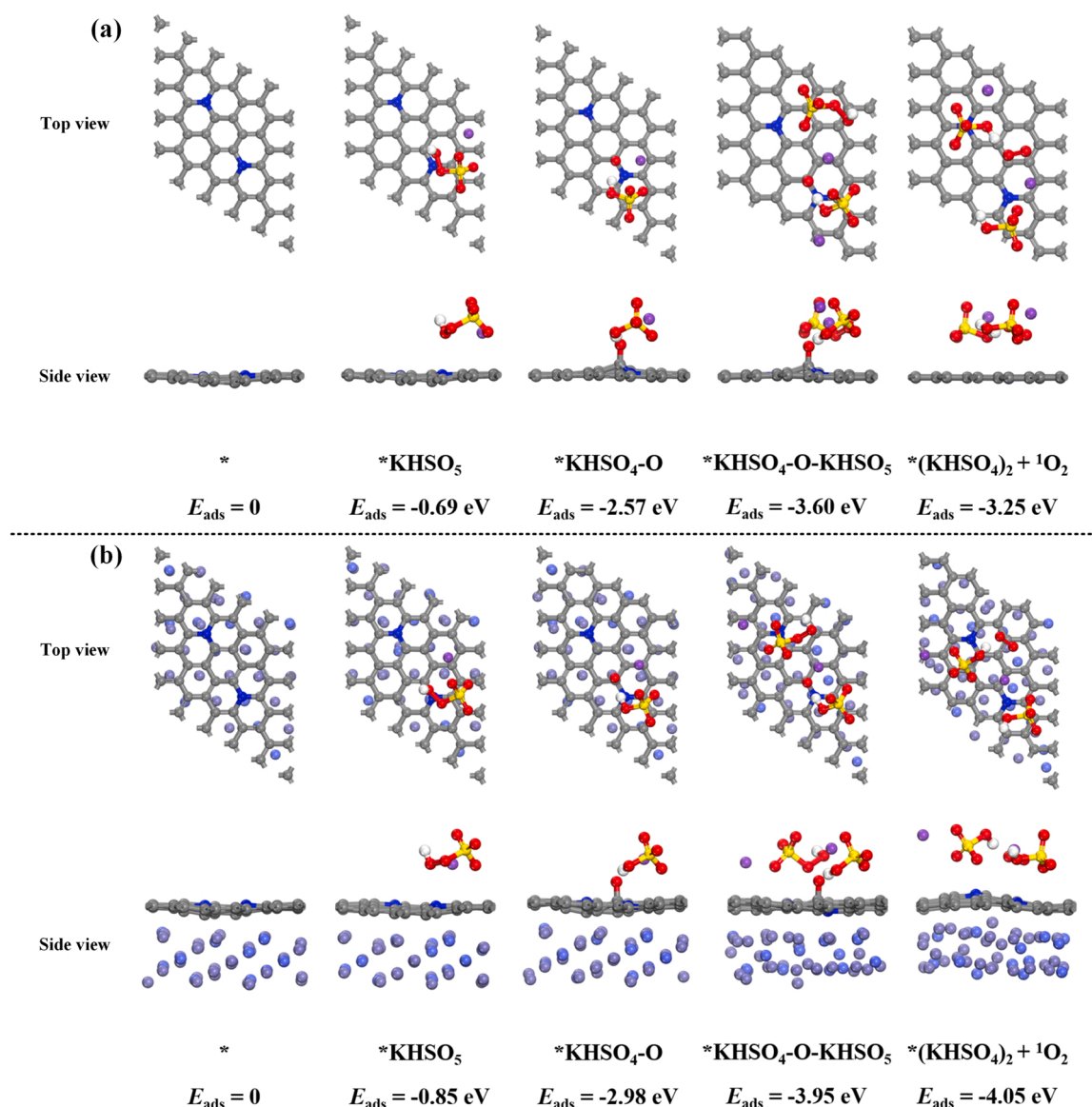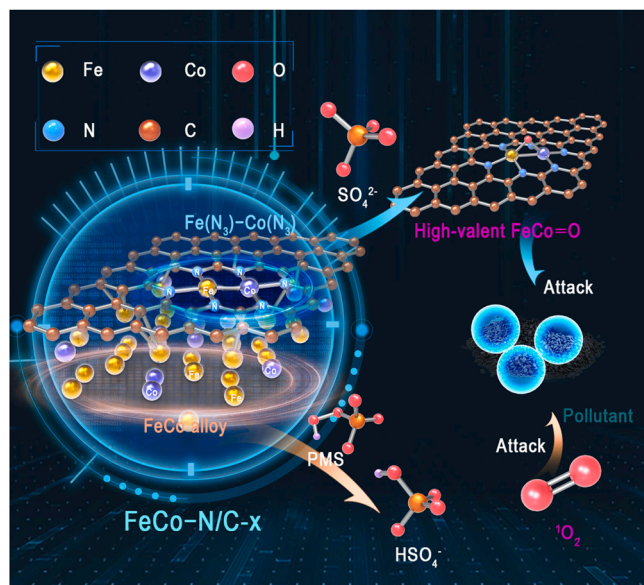


**Fig. 5.** Optimized geometric structure of adsorption configuration of PMS on (a) N/C model and (b) FeCo alloy doped N/C model and calculated adsorption energy.

**Scheme 1.** Dual active sites-dependent PMS activation mechanism over FeCo−N/C-x.

actual waters such as Qizhen Lake and West Lake (Fig. S32), further reflecting the practical application prospects of the FeCo−N/C-3/PMS system.

## 4. Conclusion

In this study, a series of FeCo−N/C-x DAMCs were prepared by precisely regulating the metal content of the precursors via a facile condensation–carbonation process. Compared with traditional metal-free N/C, single-atom Fe−N/C and Co−N/C, the as-prepared FeCo−N/C-x catalysts have higher metal loading and unique dual active sites containing $Fe(N_3)$−$Co(N_3)$ moiety and FeCo alloy without obvious aggregation problem, thereby exhibiting higher Fenton-like catalytic activity for PN degradation by PMS activation. The $Fe(N_3)$−$Co(N_3)$ moiety is beneficial for the cleavage of O−O bond and enables the formation of high-valent FeCo═O species, while the FeCo alloy simultaneously facilitates the PMS adsorption via enhanced electron transfer, thus promoting the PMS self-decomposition for the generation of $^1O_2$. The considerably high metal loading and constructed dual active sites on DAMCs positively induce the generation of high-valent FeCo═O species and $^1O_2$ by PMS activation, which is of great significance to greatly improve the Fenton-like catalytic efficiency. This study provides a novel platform for enhanced Fenton-like catalysis by increasing active metal loading and realizing the co-existence of dual active sites on DAMCs.

## CRediT authorship contribution statement

**Zhao Zhendong:** Conceptualization, Methodology, Investigation, Data curation, Visualization, Writing – original draft preparation. **Zhou Wenjun:** Supervision, Funding acquisition. **Lin Daohui:** Writing – review & editing. **Zhu Lizhong:** Project administration. **Xing Baoshan:** Writing – review & editing. **Liu Zhiqi:** Software.
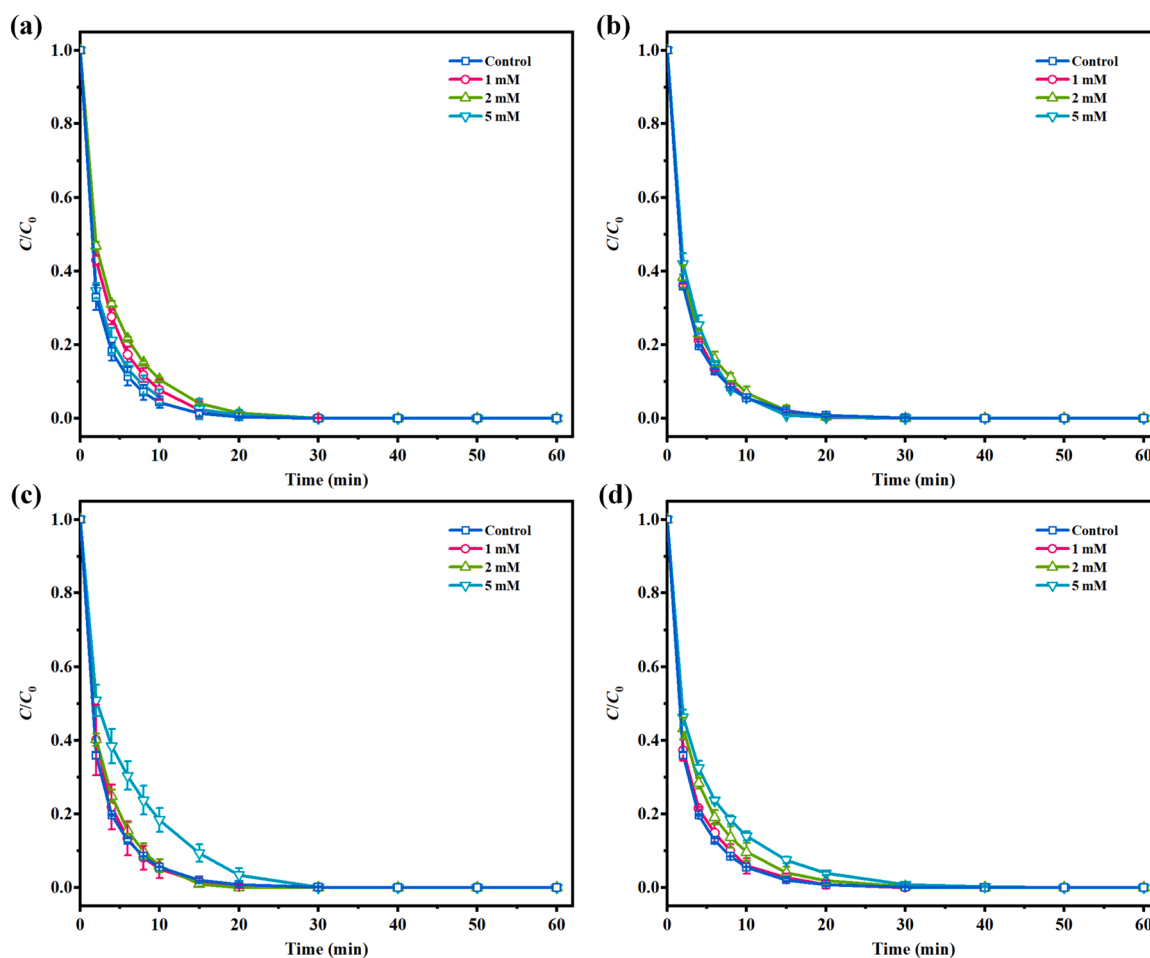


**Fig. 6.** Effect of (a) $Cl^-$, (b) $NO_3^-$, (c) $HCO_3^-$, and (d) HA on PN degradation in the FeCo−N/C-3/PMS system. Reaction condition: [PN] = 0.163 mM, [FeCo−N/C-3] = 0.05 g $L^{-1}$, [PMS] = 0.4 g $L^{-1}$, $T$ = 298 K, initial pH = 7.

## Declaration of Competing Interest

The authors declare that they have no known competing financial interests or personal relationships that could have appeared to influence the work reported in this paper.

## Acknowledgements

## Appendix A. Supporting information

Supplementary data associated with this article can be found in the online version at doi:10.1016/j.apcatb.2022.121256.

## References

[1] Y. Chen, G. Zhang, H. Liu, J. Qu, Confining free radicals in close vicinity to contaminants enables ultrafast Fenton-like processes in the interspacing of MoS$_2$ membranes, Angew. Chem. Int. Ed. 58 (2019) 8134–8138.

[2] M. Xie, F. Dai, J. Li, X. Dang, J. Guo, W. Lv, Z. Zhang, X. Lu, Tailoring the electronic metal–support interactions in supported atomically dispersed gold catalysts for efficient Fenton-like reaction, Angew. Chem. Int. Ed. 60 (2021) 14370–14375.

[3] Z. Guo, C. Li, M. Gao, X. Han, Y. Zhang, W. Zhang, W. Li, Mn−O covalency governs the intrinsic activity of Co−Mn spinel oxides for boosted peroxymonosulfate activation, Angew. Chem. Int. Ed. 60 (2021) 274–280.

[4] Y. Bu, H. Li, W. Yu, Y. Pan, L. Li, Y. Wang, L. Pu, J. Ding, G. Gao, B. Pan, Peroxydisulfate activation and singlet oxygen generation by oxygen vacancy for degradation of contaminants, Environ. Sci. Technol. 55 (2021) 2110–2120.

[5] H. Li, C. Shan, B. Pan, Fe(III)-doped g-C$_3$N$_4$ mediated peroxymonosulfate activation for selective degradation of phenolic compounds via high-valent iron-oxo species, Environ. Sci. Technol. 52 (2018) 2197–2205.

[6] Y. Liu, J. Luo, L. Tang, C. Feng, J. Wang, Y. Deng, H. Liu, J. Yu, H. Feng, J. Wang, Origin of the enhanced reusability and electron transfer of the carbon-coated Mn$_3$O$_4$ nanocube for persulfate activation, ACS Catal. 10 (2020) 14857–14870.

[7] Y. Shang, X. Xu, B. Gao, S. Wang, X. Duan, Single-atom catalysis in advanced oxidation processes for environmental remediation, Chem. Soc. Rev. 5 (2021) 5281–5322.

[8] Y. Gao, C. Yang, M. Zhou, C. He, S. Cao, Y. Long, S. Li, Y. Lin, P. Zhu, C. Cheng, Transition metal and metal–N$_x$ codoped MOF-derived Fenton-like catalysts: a comparative study on single atoms and nanoparticles, Small 16 (2020), 2005060.

[9] Y. Gao, X. Duan, B. Li, Q. Jia, Y. Li, X. Fan, F. Zhang, G. Zhang, S. Wang, W. Peng, Fe containing template derived atomic Fe–N–C to boost Fenton-like reaction and charge migration analysis on highly active Fe–N$_4$ sites, J. Mater. Chem. A 9 (2021) 14793–14805.

[10] J. He, Y. Wan, W. Zhou, ZIF-8 derived Fe–N coordination moieties anchored carbon nanocubes for efficient peroxymonosulfate activation via non-radical pathways: Role of FeN$_x$ sites, J. Hazard. Mater. 405 (2021), 124199.

[11] N. Jiang, H. Xu, L. Wang, J. Jiang, T. Zhang, Nonradical oxidation of pollutants with single-atom-Fe(III)-activated persulfate: Fe(V) being the possible intermediate oxidant, Environ. Sci. Technol. 54 (2020) 14057–14065.

[12] X. Li, X. Huang, S. Xi, S. Miao, J. Ding, W. Cai, S. Liu, X. Yang, H. Yang, J. Gao, J. Wang, Y. Huang, T. Zhang, B. Liu, Single cobalt atoms anchored on porous N-doped graphene with dual reaction sites for efficient Fenton-like catalysis, J. Am. Chem. Soc. 140 (2018) 12469–12475.

[13] L. Zhang, X. Jiang, Z. Zhong, L. Tian, Q. Sun, Y. Cui, X. Lu, J. Zou, S. Luo, Carbon nitride supported high-loading Fe single-atom catalyst for activation of peroxymonosulfate to generate $^1$O$_2$ with 100% selectivity, Angew. Chem. Int. Ed. 60 (2021) 21751–21755.

[14] Y. Gao, Y. Zhu, T. Li, Z. Chen, Q. Jiang, Z. Zhao, X. Liang, C. Hu, Unraveling the high-activity origin of single-atom iron catalysts for organic pollutant oxidation via peroxymonosulfate activation, Environ. Sci. Technol. 55 (2021) 8318–8328.

[15] K. Qian, H. Chen, W. Li, Z. Ao, Y. Wu, X. Guan, Single-atom Fe catalyst outperforms its homogeneous counterpart for activating peroxymonosulfate to achieve effective degradation of organic contaminants, Environ. Sci. Technol. 55 (2021) 7034–7043.

[16] G. Sun, Z. Zhao, R. Mu, S. Zha, L. Li, S. Chen, K. Zang, J. Luo, Z. Li, S. Purdy, A. Kropf, J. Miller, L. Zeng, J. Gong, Breaking the scaling relationship via thermally stable Pt/Cu single atom alloys for catalytic dehydrogenation, Nat. Commun. 9 (2018).

[17] Y. Pan, C. Zhang, Z. Liu, C. Chen, Y. Li, Structural regulation with atomic-level precision: from single-atomic site to diatomic and atomic interface catalysis, Matter 2 (2020) 78–110.

[18] L. Peng, X. Duan, Y. Shang, B. Gao, X. Xu, Engineered carbon supported single iron atom sites and iron clusters from Fe-rich enteromorpha for Fenton-like reactions via nonradical pathways, Appl. Catal. B Environ. 287 (2021), 119963.

[19] J. Zhang, Q. Huang, J. Wang, J. Wang, J. Zhang, Y. Zhao, Supported dual-atom catalysts: preparation, characterization, and potential applications, Chin. J. Catal. 41 (2020) 783–798.

[20] W. Ren, X. Tan, W. Yang, C. Jia, S. Xu, K. Wang, S. Smith, C. Zhao, Isolated diatomic Ni-Fe metal-nitrogen sites for synergistic electroreduction of CO$_2$, Angew. Chem. Int. Ed. 58 (2019) 6972–6976.

[21] M. Kuang, Q. Wang, P. Han, G. Zheng, Cu, Co-embedded N-enriched mesoporous carbon for efficient oxygen reduction and hydrogen evolution reactions, Adv. Energy Mater. 7 (2017), 1700193.

[22] L. Zhang, G. Fan, W. Xu, M. Yu, L. Wang, Z. Yan, F. Cheng, Isolated diatomic Zn–Fe in N-doped carbon for electrocatalytic nitrogen reduction to ammonia, Chem. Commun. 56 (2020) 11957–11960.

[23] J. Wang, Z. Huang, W. Liu, C. Chang, H. Tang, Z. Li, W. Chen, C. Jia, T. Yao, S. Wei, Y. Wu, Y. Li, Design of N-coordinated dual-metal sites: A stable and active Pt-free catalyst for acidic oxygen reduction reaction, J. Am. Chem. Soc. 139 (2017) 17281–17284.

[24] Z. Lu, B. Wang, Y. Hu, W. Liu, Y. Zhao, R. Yang, Z. Li, J. Luo, B. Chi, Z. Jiang, M. Li, S. Mu, S. Liao, J. Zhang, X. Sun, An isolated zinc–cobalt atomic pair for highly active and durable oxygen reduction, Angew. Chem. Int. Ed. 58 (2019) 2622–2626.

[25] J. Lee, U. Gunten, J. Kim, Persulfate-based advanced oxidation: critical assessment of opportunities and roadblocks, Environ. Sci. Technol. 54 (2020) 3064–3081.

[26] B. Liu, H. Shioyama, T. Akita, Q. Xu, Metal-organic framework as a template for porous carbon synthesis, J. Am. Chem. Soc. 130 (2008) 5390–5391.

[27] Y. Kaneti, J. Tang, R. Salunkhe, X. Jiang, A. Yu, K. Wu, Y. Yamauchi, Nanoarchitectured design of porous materials and nanocomposites from metal-organic frameworks, Adv. Mater. 29 (2017), 1604898.

[28] J. Yang, D. Zeng, J. Li, L. Dong, W. Ong, Y. He, A highly efficient Fenton-like catalyst based on isolated diatomic Fe-Co anchored on N-doped porous carbon, Chem. Eng. J. 404 (2021), 126376.

[29] G. Kresse, D. Joubert, From ultrasoft pseudopotentials to the projector augmented-wave method, Phys. Rev. B 59 (1999) 1758–1775.

[30] W. Kohn, L. Sham, Self-consistent equations including exchange and correlation effects, Phys. Rev. 140 (1965) 1133.

[31] M. Payne, M. Teter, D. Allan, T. Arias, J. Joannopoulos, Iterative minimization techniques for ab initio total-energy calculations: molecular dynamics and conjugate gradients, Rev. Mod. Phys. 64 (1992) 1045–1097.

[32] G. Kresse, J. Furthmuller, Efficient iterative schemes for ab initio total-energy calculations using a plane-wave basis set, Phys. Rev. B 54 (1996) 11169–11186.

[33] X. Liu, L. Wang, P. Yu, C. Tian, F. Sun, J. Ma, W. Li, H. Fu, A stable bifunctional catalyst for rechargeable zinc-air batteries: iron–cobalt nanoparticles embedded in a nitrogen-doped 3D carbon matrix, Angew. Chem. Int. Ed. 57 (2018) 16166–16170.

[34] P. Yin, T. Yao, Y. Wu, L. Zheng, Y. Lin, W. Liu, H. Ju, J. Zhu, X. Hong, Z. Deng, G. Zhou, S. Wei, Y. Li, Single cobalt atoms with precise N-coordination as superior oxygen reduction reaction catalysts, Angew. Chem. Int. Ed. 55 (2016) 10800–10805.

[35] Y. Wang, A. Kumar, M. Ma, Y. Jia, Y. Wang, Y. Zhang, G. Zhang, X. Sun, Z. Yan, Hierarchical peony-like FeCo-NC with conductive network and highly active sites as efficient electrocatalyst for rechargeable Zn-air battery, Nano Res. 13 (2020) 1090–1099.

[36] X. Mi, P. Wang, S. Xu, L. Su, H. Zhong, H. Wang, Y. Li, S. Zhan, Almost 100% peroxymonosulfate conversion to singlet oxygen on single-atom CoN$_{2+2}$ sites, Angew. Chem. Int. Ed. 60 (2021) 4588–4593.

[37] X. Long, Z. Li, G. Gao, P. Sun, J. Wang, B. Zhang, J. Zhong, Z. Jiang, F. Li, Graphitic phosphorus coordinated single Fe atoms for hydrogenative transformations, Nat. Commun. 11 (2020).

[38] S. Zhu, X. Huang, F. Ma, L. Wang, X. Duan, S. Wang, Catalytic removal of aqueous contaminants on N-doped graphitic biochars: inherent roles of adsorption and nonradical mechanisms, Environ. Sci. Technol. 52 (2018) 8649–8658.

[39] G. Buxton, C. Greenstock, W. Helman, A. Ross, Critical-review of rate constants for reactions of hydrated electrons, hydrogen atoms and hydroxyl radicals ($^\cdot$OH/$^\cdot$O$^-$) in aqueous solution, J. Phys. Chem. Ref. Data 17 (1988) 513–886.

[40] P. Neta, R. Huie, A. Ross, Rate constants for reactions of inorganic radicals in aqueous solution, J. Phys. Chem. Ref. Data 17 (1988) 1027–1284.

[41] W. Haag, J. Hoigne, Singlet oxygen in surface waters. 3. Photochemical formation and steady-state concentrations in various types of waters, Environ. Sci. Technol. 20 (1986) 341–348.

[42] L. Wu, B. Li, Y. Li, X. Fan, F. Zhang, G. Zhang, Q. Xia, W. Peng, Preferential growth of the cobalt (200) facet in Co@N–C for enhanced performance in a Fenton-like reaction, ACS Catal. 11 (2021) 5532–5543.

[43] J. Moan, E. Wold, Detection of singlet oxygen production by ESR, Nature 279 (1979) 450–451.

[44] E. Yun, J. Lee, J. Kim, H. Park, J. Lee, Identifying the nonradical mechanism in the peroxymonosulfate activation process: singlet oxygenation versus mediated electron transfer, Environ. Sci. Technol. 52 (2018) 7032–7042.

[45] J. Zhu, F. Yu, J. Meng, B. Shao, H. Dong, W. Chu, T. Cao, G. Wei, H. Wang, X. Guan, Overlooked role of Fe(IV) and Fe(V) in organic contaminant oxidation by Fe(VI), Environ. Sci. Technol. 54 (2020) 9702–9710.

[46] Y. Gao, Y. Zhou, S. Pang, J. Jiang, Z. Yang, Y. Shen, Z. Wang, P. Wang, L. Wang, New insights into the combination of permanganate and bisulfite as a novel advanced oxidation process: Importance of high valent manganese-oxo species and sulfate radical, Environ. Sci. Technol. 53 (2019) 3689–3696.

[47] Y. Zong, X. Guan, J. Xu, Y. Feng, Y. Mao, L. Xu, H. Chu, D. Wu, Unraveling the overlooked involvement of high-valent cobalt-oxo species generated from the cobalt(II)-activated peroxymonosulfate process, Environ. Sci. Technol. 54 (2020) 16231–16239.

[48] B. Shao, H. Dong, B. Sun, X. Guan, Role of ferrate(IV) and ferrate(V) in activating ferrate(VI) by calcium sulfite for enhanced oxidation of organic contaminants, Environ. Sci. Technol. 53 (2019) 894–902.

[49] O. Pestovsky, S. Stoian, E. Bominaar, X. Shan, E. Münck, L. Que, A. Bakac, Aqueous Fe$^{IV}$=O: Spectroscopic identification and oxo-group exchange, Angew. Chem. Int. Ed. 44 (2005) 6871–6874.

[50] X. Xue, K. Hanna, C. Despas, F. Wu, N. Deng, Effect of chelating agent on the oxidation rate of PCP in the magnetite/H$_2$O$_2$ system at neutral pH, J. Mol. Catal. A: Chem. 311 (2009) 29–35.

[51] Y. Zhou, J. Jiang, Y. Gao, J. Ma, S. Pang, J. Li, X. Lu, L. Yuan, Activation of peroxymonosulfate by benzoquinone: a novel nonradical oxidation process, Environ. Sci. Technol. 49 (2015) 12941–12950.

[52] D. Sawyer, J. Valentine, How super is superoxide? Acc. Chem. Res. 14 (1981) 393–400.

[53] D. Evans, M. Upton, Studies on singlet oxygen in aqueous solution. Part 3. The decomposition of peroxy-acids, J. Chem. Soc. Dalton Trans. 6 (1985) 1151–1153.

[54] P. Eyer, Effects of superoxide dismutase on the autoxidation of 1,4-hydroquinone, Chem. Biol. Interactions 80 (1991) 159–176.

[55] J. You, C. Zhang, Z. Wu, Z. Ao, W. Sun, Z. Xiong, S. Su, G. Yao, B. Lai, N-doped graphite encapsulated metal nanoparticles catalyst for removal of Bisphenol A via activation of peroxymonosulfate: a singlet oxygen-dominated oxidation process, Chem. Eng. J. 415 (2021), 128890.